Impact of small-scale saline tracer heterogeneity on electrical resistivity monitoring in fully and partially saturated porous media: insights from geoelectrical milli-fluidic experiments

Damien Jougnot[1], Joaquín Jiménez-Martínez[2,3], Raphaël Legendre[4], Tanguy Le Borgne[4], Yves Méheust[4], and Niklas Linde[5]

[1]*Sorbonne Université, CNRS, EPHE, UMR 7619 METIS, Paris, France.*
[2]*Department Water Resources and Drinking Water, Swiss Federal Institute of Aquatic Science and Technology, EAWAG, Dubendorf, Switzerland.*
[3]*Department of Civil, Environmental and Geomatic Engineering, ETH Zurich, Zurich, Switzerland.*
[4]*Géosciences Rennes (UMR CNRS 6118), University of Rennes 1, Rennes, France.*
[5]*Applied and Environmental Geophysics Group, Institute of Earth Sciences, University of Lausanne, Switzerland.*

This paper is published in Advance in Water Resources, please cite as:
D. Jougnot, J. Jiménez-Martínez, R. Legendre, T. Le Borgne, Y. Méheust, N. Linde (2018) Impact of small-scale saline tracer heterogeneity on electrical resistivity monitoring in fully and partially saturated porous media: insights from geoelectrical milli-fluidic experiments, Advances in Water Resources, 113, 295-309, doi:10.1016/j.advwatres.2018.01.014

Abstract

Time-lapse electrical resistivity tomography (ERT) is a geophysical method widely used to remotely monitor the migration of electrically-conductive tracers and contaminant plumes in the subsurface. Interpretations of time-lapse ERT inversion results are generally based on the assumption of a homogeneous solute concentration below the resolution limits of the tomogram depicting inferred electrical conductivity variations. We suggest that ignoring small-scale solute concentration variability (i.e., at the sub-resolution scale) is a major reason for the often-observed apparent loss of solute mass in ERT tracer studies. To demonstrate this, we developed a geoelectrical millifluidic setup where the bulk electric conductivity of a 2D analogous porous medium, consisting of cylindrical grains positioned randomly inside a Hele-Shaw cell, is monitored continuously in time while saline tracer tests are performed through the medium under fully and partially saturated conditions. High resolution images of the porous medium are recorded with a camera at regular time intervals, and provide both the spatial distribution of the fluid phases (aqueous solution and air), and the saline solute concentration field (where the solute consists of a mixture of salt and fluorescein, the latter being used as a proxy for the salt concentration). Effective bulk electrical conductivities computed numerically from the measured solute concentration field and the spatial distributions of fluid phases agree well with the measured bulk conductivities. We find that the effective bulk electrical conductivity is highly influenced by the connectivity of high electrical conductivity regions. The spatial distribution of air, saline tracer fingering, and mixing phenomena drive temporal changes in the effective bulk electrical conductivity by creating preferential paths or barriers for electrical current at the pore-scale. The resulting heterogeneities in the solute concentrations lead to strong anisotropy of the effective bulk electrical conductivity, especially for partially saturated conditions. We highlight how these phenomena contribute to the typically large apparent mass loss observed when conducting field-scale time-lapse ERT.

Keywords: Hydrogeophysics, Petrophysics, Millifluidics, Electrical Conductivity, Unsaturated Flow, Tracer test, Transport in Porous Media, Anisotropy

1 Introduction

Geophysical methods are increasingly used in subsurface hydrology. Their main advantages lie in their largely non-invasive nature, their sensitivity to properties of interest, and in that they provide images of the subsurface at a comparatively high spatial resolution (e.g., Hubbard and Rubin, 2005; Guérin, 2005; Binley et al., 2006; Hubbard and Linde, 2011; Binley et al., 2015). A particular emphasis has been given to geophysical methods with responses that depend on the electrical resistivity (or the electrical conductivity, its inverse) because electrical resistivity is sensitive to sub-surface properties such as: the lithology (porosity, tortuosity, specific surface area), the presence of fluids in the pore space (water saturation and its spatial distribution), and the pore fluid chemistry (ionic concentrations). The links between physical properties (electrical resistivity) and hydrological properties and state variables of interest are described by petrophysical relationships (for literature reviews, see Hubbard and Linde, 2011; Glover, 2015, among others).

Resistivity methods can be applied to a wide range of scales, from the laboratory (on centimetric samples) to the field (up to several kilometers). Measurements are achieved by driving a known electrical current between an electrode pair while measuring the resulting voltage between another electrode pair. The electrical resistivity structure of the subsurface can be inferred by electrical resistivity tomography (ERT), which is an inversion process that uses measured electrical resistances from multiple current injection and voltage pairs (e.g., Binley and Kemna, 2005). If the measurement process is repeated in time, it is possible to perform time-lapse inversion and, thus, to track temporally-varying processes in the subsurface (e.g., Revil et al., 2012). Time-lapse ERT has been widely applied under both saturated (e.g., Kemna et al., 2002; Singha and Gorelick, 2005; Pollock and

Cirpka, 2012) and partially saturated conditions (e.g., Daily et al., 1992; Binley et al., 2002; Looms et al., 2008; Haarder et al., 2015) using electrodes placed on the ground or in boreholes.

Geophysical data have a limited resolving power, which implies that geophysical tomograms are best understood as spatially-filtered representations of subsurface properties (e.g., Menke, 1989; Friedel, 2003). The “filter width" is often referred to as the resolution and it varies in space and time as a function of experimental design, noise, the actual electrical conductivity distribution and choices made when developing or running an inversion algorithm. In ERT studies, the resolution decreases (the filter width increases) when the distance between the electrodes and the target of interest increase. Day-Lewis et al. (2005) highlight the inherent resolution limitations of cross-borehole ERT through a careful numerical and theoretical study. The limited resolution of ERT tomograms can (if ignored) lead to important errors when translating inferred resistivity to properties of interest through petrophysical relationships (e.g., Singha and Gorelick, 2006; Looms et al., 2008; Rosas-Carbajal et al., 2015; Haarder et al., 2015). For instance, a common problem is the apparent loss of mass occurring in field-based experiments when comparing ERT-inferred mass to the actual injected water volume or mass of salt. For example, Binley et al. (2002) noticed an apparent water mass loss of 50 $\%$ when monitoring a fluid tracer in the vadose zone. Using a saline tracer in the fully saturated part of an aquifer, Singha and Gorelick (2005) only “recovered" 25$\%$ of the mass using ERT data. They demonstrate that this apparent tracer mass loss is more important when the target volume is small and the electrical conductivity contrast is high. In a synthetic 3-D time-lapse study mimicking an actual field experiment, Doetsch et al. (2012) obtained a mass recovery close to 80 $\%$, while the corresponding field experiment provided an ERT-inferred mass recovery between 10 $\%$ and 25 $\%$. The authors attribute this discrepancy to the fact that classical smoothness-constrained inversions (often referred to as Occam’s inversion Constable et al., 1987) will, by construction, seek the smoothest model that fits the data. Due to the upscaling (averaging) process inherent to electrical current flow, less tracer mass is needed to explain ERT data when a heterogeneous plume is represented by a larger plume of near-uniform concentration. Doetsch et al. (2012) suggest that this apparent mass loss could potentially be used as an indicator of the tracer plume heterogeneity at scales below the resolution of the tomograms. Effects of such small-scale solute concentrations are commonly ignored and it is implicitly assumed that the solution is perfectly mixed below this scale. A few studies have considered anomalous transport and the effect of small-scale heterogeneities on petrophysical relationships (e.g., Singha et al., 2007, 2008; Swanson et al., 2015). For example, Singha et al. (2007), Briggs et al. (2013, 2014), and Day-Lewis et al. (2017) have proposed dual-domain approaches to account for this phenomenon.

The question of how field-scale studies are impacted by sub-resolution flow and transport processes is deeply tied to the physics of these processes. For example, unsaturated flows give rise to gravitational (Glass and Nicholl, 1996) and viscous (Méheust et al., 2002; Toussaint et al., 2012; Ferrari and Lunati, 2013) interface instabilities leading to sub-Darcy-scale fingering. It is now well understood that this fingering is the main reason why Darcy-scale modelling of flows in the unsaturated zone should consider a dependence of the capillary pressure on the local Darcy velocity (Løvoll et al., 2011) (Hassanizadeh et al., 2002, the so-called dynamic capillary pressure). This strong pore-scale heterogeneity of the flow, in particular for unsaturated flows, is associated with preferential paths for solute transport and incomplete solute mixing at the pore-scale Jiménez-Martínez et al. (2015, 2017). Incomplete mixing (e.g., Dentz et al., 2011; Le Borgne et al., 2011) and strong heterogeneties of the advection paths for solutes (as observed also at larger scales (e.g., Seyfried and Rao, 1987; Koestel and Larsbo, 2014), result in anomalous transport that makes Fickian models unsuitable at the Darcy scale and at the block scale corresponding to the grid size used for numerical simulations Jiménez-Martínez et al. (2017). Geophysical monitoring data of solute transport and mixing processes are also likely impacted by such mechanisms acting at sub-resolution scales.

Recent advances in milli- and micro-fluidic laboratory experiments provide means to better understand and predict pore-scale transport properties and mixing in saturated (e.g., Willingham et al., 2008; de Anna et al., 2013) and partially saturated porous media (e.g., Jiménez-Martínez et al., 2015,

2017). In a pioneering work, Kozlov et al. (2012) investigate the validity and limitations of a classical petrophysical relationship involving electrical conductivity in a porous micro-model filled by water and oil, but without considering solute transport. The present work builds on the experimental developments of Jiménez-Martínez et al. (2015, 2017) and aims to study the effect of the spatial distribution of phases and solute concentration field on the bulk electrical resistivity below the ERT resolution. This is the first time a laboratory pore-scale fluorimetric flow and transport experiment is equipped with geoelectrical monitoring capabilities.

The manuscript is organized as follows: in section 2 we present our geoelectrical milli-fluidic experimental setup; we then explain the image treatment and the numerical modeling of the electrical problem (section 3); finally, we present and discuss in section 4 the results that we have obtained from tracer tests under fully-saturated and partially-saturated conditions, and how these results can be used to gain insights into how upscaled bulk electrical resistivity is affected by sub-resolution heterogeneity and processes.

2 Experimental method

2.1 Milli-fluidic setup for spatially-resolved pore-scale fluorimetry

We build on the recent experimental developments by de Anna et al. (2013) and Jiménez-Martínez et al. (2015, 2017) and consider a 2D analogous porous medium which we refer to as the flow cell (Fig. 1). Using such a setup, it is possible to measure the spatial distribution of the fluids in the cell and the ionic concentration field in the liquid (wetting) phase using a fluorimetry technique. A light source is placed below the cell (Fig. 1a) and the cell is monitored using a high-resolution camera (27 pixels per mm, 12 bit images), positioned 32 cm above the flow cell with its axis normal to the horizontal mean plane of the cell. The light source excites the fluorescent tracer present in the wetting solution; the tracer consequently emits light around a given wavelength, which is recorded by the camera. A filter placed on the light source prevents light with wavelengths belonging to the emission range of fluorescein to go through the flow cell, while a band-pass filter located in front of the camera allows the light intensity corresponding only to the fluorescein excitation to be recorded. We can thus track the spatial distribution of the fluids (air and water) phases. Furthermore, as the intensity of the light recorded on a given pixel of the camera sensor depends on the mean fluorescein concentration probed along the direction between the light source and the sensor, the spatial distribution of the intensity recorded on an image provides a measure of the 2D spatial distribution of the fluorescein (or fluorescein concentration field) within the liquid phase. By fixing a concentration ratio between the fluorescein and another ionic species having a similar diffusion coefficients (NaCl in this study), it is possible to infer the concentration field of the salt from that of the fluorescein. For this study, the camera monitoring system (MegaPlus EP11000, Princeton Instruments) was set to take 1 picture every 2 s to capture the fluid phases and solute dynamics in the flow cell.

The flow cell consists of a single layer of 4500 cylindrical solid grains positioned between two parallel transparent plates separated by a distance equal to the cylinders' height. It is built by soft lithography as follow. Two glass plates are separated by the desired distance using spacers. The space between them is filled with a UV-sensitive polymer (NOA-81). The photomask (resulting from a numerical model of the 2D compaction of circular grains with diameters distributed according to a Gaussian law of prescribed standard deviation) is then placed on top of the top plate. The mask is transparent where solid grains are to be found, opaque everywhere else. The light coming from the collimated 365 nm UV source passes through the transparent disks in the mask, polymerizing the NOA-81 and giving rise to solid cylindrical grains spanning the vertical gap between the two glass plates. The remnant uncured, still liquid, polymer material is cleaned by flowing through ethanol. The resulting 2-D porous medium is water-wet.

The geometry used herein corresponds to the so-called homogeneous geometry used by Ferrari

et al. (2015). The flow cell is closed on two of its lateral sides (facing each other), while the two other lateral sides remain open and constitute the inlet and outlet of the cell. Its length, defined between the inlet and outlet, is 140 mm, its width is 92 mm, and its thickness (equal to the cylinder height) is 0.5 mm (see Jiménez-Martínez et al., 2015, for details). The cell is positioned with the glass plates lying horizontal. The vertically-oriented cylindrical grains act as obstacles for the flow of fluids in the cell (Fig. 1a). This 2D geometry has a cross-sectional area of 43.64 mm^2 in the direction normal to the average flow direction and typical pore throat and pore sizes of 1.07 mm and 1.75 mm, respectively. It yields a permeability of 4.32×10^{-9} m^2.

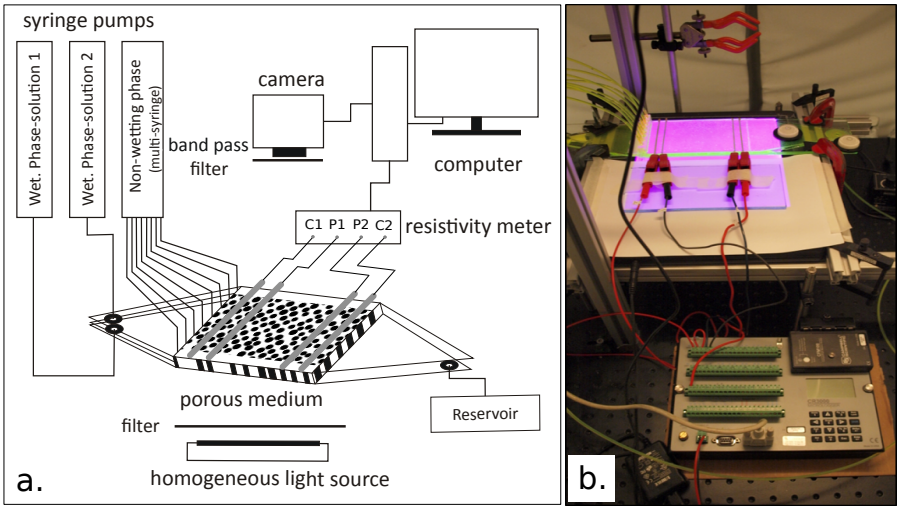

Figure 1: (a) Overall scheme of the setup for the fluorimetric study in the 2D porous medium, featuring the injection systems for air (non-wetting fluid phase), the tracer solution (wetting phase 1), and the background solution (wetting phase 2), as well as the camera and the electrical resistivity monitoring system (modified from Jiménez-Martínez et al., 2015). (b) Photography of the geoelectrical milli-fluidic setup.

The cell is connected to three reservoirs upstream that contain wetting and non-wetting fluids, and to an outlet reservoir downstream. The fluids are injected in the flow cell with syringe pumps at a controlled flow rate. The non-wetting phase is air (Fig. 1a) and the wetting (i.e., liquid) phase is a 60-40 $\%$ by weight distilled water/glycerol solution (see Jiménez-Martínez et al., 2015). The glycerol increases the viscosity of the solution ($\mu_w = 3.78 \times 10^{-2}$ Pa s), thereby increasing the viscosity ratio between the wetting and non-wetting phases, and slowing down molecular diffusion. The wetting phase solutions 1 and 2 have different mass concentrations of NaCl salt (C_{NaCl}) and fluorescein (C_{fluo}). These solutions are labeled “tracer" (tr) and “background" (bkg) concentrations, respectively. The mass concentration of fluorescein is ten times smaller than that of the NaCl salt (i.e., $C_{\text{NaCl}} = 10\ C_{\text{fluo}}$).

In order to relate the measured light intensity to the electrical conductivity of the solution, we first synthesized a set of ten solutions with different fluorescein/NaCl salt concentrations by successive dilutions, with C_{fluo} ranging between 701.5 and 0.0856 mg L^{-1}. The ratio of NaCl to fluorescein mass concentration is identical for all ten solutions and set to 10. The electrical conductivity of each solution was measured with a handheld electrical conductivity meter (WTW Cond 340i). Correspondingly, the light intensity of each solution was measured in a cell similar to the one used for the tracer experiments (i.e., same glass and aperture thickness) but without cylindrical pillars. For the tracer experiments, we chose the background concentration solution ($C^{\text{tr}}_{\text{fluo}}$ =5.48 mg L^{-1}) by measuring the light intensity for all the solutions and selecting the lowest concentration for which the corresponding light intensity was above the detection threshold. Then, we chose the tracer concentration to be $C^{\text{tr}}_{\text{fluo}}$ =350.8 mg L^{-1} in to avoid light saturation for the camera. It yields a background and tracer electrical conductivity of $\sigma^{\text{bkg}}_{\text{w}}$ =0.0055 and $\sigma^{\text{tr}}_{\text{w}}$ =0.213 S m^{-1}, respectively. We only kept the six so-

lutions with fluorescein mass concentrations in between these two values to establish the calibration curve. Combining these two sets of measurements and using a Piecewise Cubic Hermite Interpolating Polynomial interpolation in between the data, we obtain an empirical curve relating the measured light intensity and the electrical conductivity of the solution σ_w (in S m^{-1}) (Fig. 2).

However, when using this calibration curve to infer local solution conductivities inside the flow cell during subsequent tracer tests (which we present in section 4 below), we noticed that the largest conductivity values measured inside the cell were larger than the conductivity of the injected tracer solution. This unphysical result showed that the calibration curve obtained in the flow cell without solid grains (a standard Hele-Shaw cell), was not fully adequate for the tracer experiment cell. We have therefore assumed that a slight difference in the cell thickness, or perhaps the impact of the presence of the translucid solid grains, was responsible for the discrepancy. In particular, given the large fluorescein concentration in the injected tracer, it is not unreasonable to consider that some multiple scattering of the light emitted by the fluorescein may occur in the cell, with a fraction of the emitted light being absorbed by other fluorescein molecules on its way out from the cell, which is possible due to the overlapping emission and absorption spectra of fluorescein (see Sjöback et al., 1995). Accounting for this multiple scattering yields a prediction of the light intensity transmitted to the camera that is offset from the intensity measured in the absence of multiple scattering by a factor which is a function of the flow cell's thickness. Hence a discrepancy in the cell thicknesses would lead to exactly this type of effect. Therefore, we have corrected the recorded calibration curve by assuming that the light intensity value calibrated in the pure Hele-Shaw cell for a given tracer concentration was offset by a given factor (independent of the given tracer concentration) with respect to the correct value for the experimental cell. The correction factor of 0.805 has been inferred from the (reasonable) constraint that the maximum conductivity value measured in the cell during the experiment should exactly correspond to the conductivity of the injected tracer solution. The corrected calibration curve is used systematically when inferring local conductivities from light intensities in our experimental cell (Fig. 2).

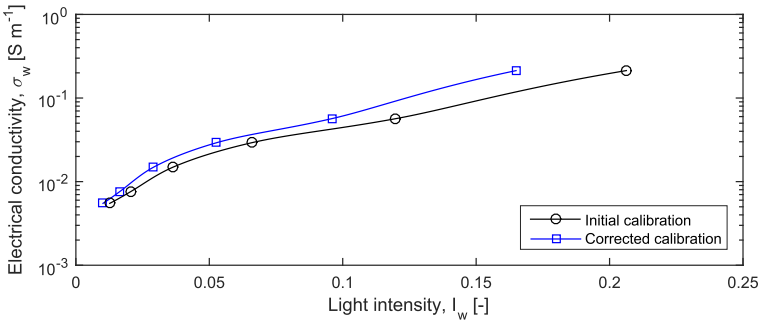

Figure 2: Initial and corrected calibration curves: pore water electrical conductivity σ_w as a function of the light intensity I_w.

2.2 Geoelectrical monitoring

The geoelectric monitoring is performed using a four electrode setup (see Schlumberger (1920) for the historical paper, and more recently Binley and Kemna (2005) for a more hydrology-oriented introductory text). We inject a current in the two outer electrodes (C1 and C2) and measure the resulting electrical voltage between the two inner electrodes (P1 and P2) (Fig. 1a). Given that the zone of investigation is localized between P1 and P2, we chose not to have equally spaced electrodes along the cell. The spacing between potential electrodes P1 and P2 is 97 mm in order to study the largest possible zone of the flow cell, while the C1-P1 and P2-C2 spacings are 8 mm (Fig. 1).

The electrodes consist of a thin layer of copper (90 μm). They were inserted at the bottom of the cylinder layer while manufacturing the cell; this ensured good contact with the fluids in the cell without perturbing the flow. We chose relatively wide electrodes, 2.5 mm for the current injection and 2 mm for the potential measurement, to ensure a low contact resistance even at low water saturation. The disadvantage of these large copper electrodes is that they block the light between the light source and the camera, which results in a loss of information about the fluid phases and concentration field located above them.

We measured the effective bulk electrical resistivity of the medium at a temporal resolution of 2 s. We used a Campbell datalogger program for a half bridge with four wires configuration (Fig. 1b). The datalogger imposes a 1 V electrical potential difference between C1 and C2 that drives an electrical current in the cell. The resulting electrical current and voltage between P1 and P2 is converted into a bulk electrical resistance R^{meas} (in Ω). In order to obtain the effective bulk electrical resistivity ρ^{meas} (in Ω m), it is then necessary to determine the geometrical factor of the cell, K_{G} (in m) such that $\rho^{\text{meas}} = K_{\text{G}} R^{\text{meas}}$. This parameter was first estimated numerically in 3D using COMSOL Multiphysics following the procedure described by Jougnot et al. (2010a) using the actual cell geometry. The resulting estimate was $K_{\text{G}} = 4.753 \times 10^{-4}$ m. For this setup, the analytical solution for the 1D case (cell aperture area divided by the spacing between the potential electrodes, see Binley and Kemna, 2005) provides a close approximation to the numerical model: $K_{\text{G}} \approx 4.766 \times 10^{-4}$ m.

2.3 Electrical characterization of the porous medium and fluid phases geometry

Prior to the tracer tests, we first characterized the porous medium and the geometry of the fluid phases from an electrical point of view, using a series of electrical measurements with different homogeneous solute concentrations. To do so, we first saturated the medium with one of the solutions obtained by dilution (i.e., with a given electrical conductivity σ_{w}). Then, we jointly inject the chosen solution (i.e., the wetting fluid) and the air (i.e., the non-wetting fluid) to partly fill the medium with air while keeping the liquid phase connected (thereby imposing partially saturated conditions). By varying the injection rates of the fluids, we reached three or more steady state flows with different saturations (i.e., proportion of wetting fluid in the porous space). By steady state flows we refer to flows for which the spatial distributions of the fluid phases change continuously, but their statistical properties (saturation, distribution of cluster sizes, see Tallakstad et al., 2009) are stationary. The steady state is considered to have been reached when the saturation fluctuates around a plateau value, and the longitudinal and transverse saturation profiles fluctuate around a uniform stationary profile. This can only be measured a posteriori, from the images. After performing measurements with the largest saturation range (S_{w}) possible with the setup and experimental protocol (i.e., $S_{\text{w}} \in [0.46\ ;\ 1]$), the procedure was repeated with another concentration of the solution (i.e., another σ_{w}). Note that the lower saturation limit is linked to the connectivity of the liquid phase and its stability overtime; liquid phase connectivity is necessary to allow measurement of the bulk electrical conductivity. During these steps, both the bulk electrical conductivity of the cell and the spatial distribution of the fluid phases were recorded. These first series of measurements provided a set of images and electrical conductivity measurements for different tracer solutions (i.e., different σ_{w}) at different saturation degrees.

2.4 Tracer test procedures

After these initial experiments, we conducted a tracer test under saturated conditions and three tracer tests under partially saturated conditions.

For the fully saturated test, the medium was first saturated with the background solution ($C_{\text{fluo}}^{\text{bkg}}$ and $\sigma_{\text{w}}^{\text{bkg}}$) to obtain a homogeneous initial state. Then, the tracer ($C_{\text{fluo}}^{\text{tr}}$ and $\sigma_{\text{w}}^{\text{tr}}$) was injected at a constant rate (1.375 mm^3 s^{-1}). The injection rate was chosen to be low enough to follow the dynamics with

the sampling frequency of our acquisition setup. It yields the dimensionless Reynolds and Péclet numbers, Re = 1.64×10^{-4} and Pe = 241, respectively. The test was stopped when the measured electrical conductivity reached a constant value (after $\sim$12500 s), that is, when an apparent steady-state was reached for the salt concentration field.

For the tracer tests performed under partially-saturated conditions, an unsaturated flow was first imposed by jointly injecting air and the background solution at constant flow rates to reach a steady-state flow as explained in section 2.3, with a given liquid saturation of the medium and a given size distribution of air clusters. After stopping the injection of air and background solution, the tracer solution was injected continuously and at a volumetric flow rate that was sufficiently low so that the impact on the previously-established air cluster was minimal (0.277 mm^3 s^{-1}, yielding Re = 3.79×10^{-4} and Pe = 68). The experiments were terminated when the measured bulk electrical conductivity of the flow cell reached a constant value (after $\sim$15200 s for the test presented in the results section).

3 Modelling approach

3.1 From images to effective bulk electrical conductivity

The experiments described in the previous section provide two kinds of data: images with a light intensity value per pixel, $I(x, y)$, on the one hand, and an effective bulk electrical conductivity of the entire cell, σ^{meas}, on the other hand. In this section, we describe how we simulate the effective bulk electrical conductivity from the images in order to compare the computed conductivity, σ^{sim}, to the measured one, σ^{meas}.

The raw images are first corrected for spatial heterogeneities in the incident light intensity (which is largest at the center of the flow cell). All subsequent data processing is performed on these corrected images. Figure 3 shows the flow chart used to process such a corrected image, and the subsequent electrical field simulations. The flow cell geometry, with the exact geometry of the borders and exact position of each cylinder, is obtained from an image of the medium saturated with a solution at $C_{\text{fluo}}^{\text{bkg}}$ and is stored as a binary image denoted "pore space mask", which defines the pore space: $I_{\text{mask}} = 0$ for pixels positioned inside borders and cylindrical grains, and 1 for pixels positioned within the pore space. The electrodes are clearly visible in the images; their positions and geometries are extracted and stored into another mask, the "electrode mask". The porosity of the medium is readily computed from the pore space mask: $\phi = 0.73$. Subsequent images (2966 $\times$ 2308 pixels) acquired during the course of the experiments are used to extract (1) the phase distribution and (2) the map of local conductivities at different times. Image pixels belonging to the air phase are identified as those for which the mask value is 1 ($I_{\text{mask}} = 1$) and the recorded light intensity is null ($I = 0$). The liquid (wetting fluid) phase is identified as consisting of pixels for which $I_{\text{mask}} = 1$ and $I > 0$; we define a light intensity map in the wetting phase, $I_{\text{w}}(x, y)$, equal to 0 outside the water phase, and to $I(x, y)$ inside the water phase. From this image processing, we can monitor the water saturation during the tests by considering the ratio of the number of pixels belonging to the water phase to the number of pixels belonging to the entire pore space. Using the corrected calibration curve discussed in section 2.1 above, we then convert the $I_{\text{w}}(x, y)$ map in to a map of local conductivities.

Using the spatial distributions of the phases and local tracer conductivities, it is possible to simulate the cell's effective electrical bulk conductivity, σ^{sim}. This numerical upscaling is based on the pixel distribution of electrical conductivity and is, therefore, limited by the image resolution. Using to the calibration relationship between σ_{w} and the light intensity obtained from the different dilutions as described in paragraph 2.1, each pixel in the image is attributed a given electrical conductivity $\sigma_{\text{w}}(x, y)$ from $I_{\text{w}}(x, y)$. The electrical conductivity of the wetting fluid ranges between $\sigma_{\text{w}} =$ 0.0041 and 0.2130 S m^{-1}. In the simulations, the electrodes were given an electrical conductivity of $\sigma_{\text{elec}} = 10^4$ S m^{-1}, which is sufficiently high to obtain practically-constant isopotential values along

the electrodes but also small enough to avoid numerical problems. The polymer NOA81 (cylinders and borders) is, similarly to the air phase, a non-conducting material and an arbitrary low electrical conductivity is assigned to both: $\sigma_{\text{NOA81}} = \sigma_{\text{air}} = 10^{-6}$ S m^{-1}, which is a value sufficiently low to avoid significant electrical current flow in these materials while allowing convergence of the numerical code. These electrical simulations will help understand exactly where the electrical current is flowing and its links with solute transport processes.

The numerical upscaling of the electrical conductivity consists in solving the Poisson equation in 2D. We use a modified version of the code MaFlot (www.maflot.com) initially designed to address density-driven Darcy flows Künze and Lunati (2012). In the simulations, we generate the current flow by imposing an electrical voltage of 1 V between the current electrode (C1 and C2) (see Fig. 1). The top and bottom boundary conditions are set to electrical insulation. The electrical problem is therefore a boundary problem that can be seen as an analog to determining the effective hydraulic conductivity of a porous medium of heterogeneous permeability field between two reservoirs with a given pressure difference under steady state conditions. Note that imposing a potential difference in the modelling instead of injecting a fixed electrical current presents two main advantages: (1) it corresponds to what is done experimentally and (2) it avoids problems related to air clusters on the electrodes. Indeed, injecting a fixed current would require a perfect knowledge of the wetting phase and solute concentration above the electrode, which is impossible with the present experimental setup.

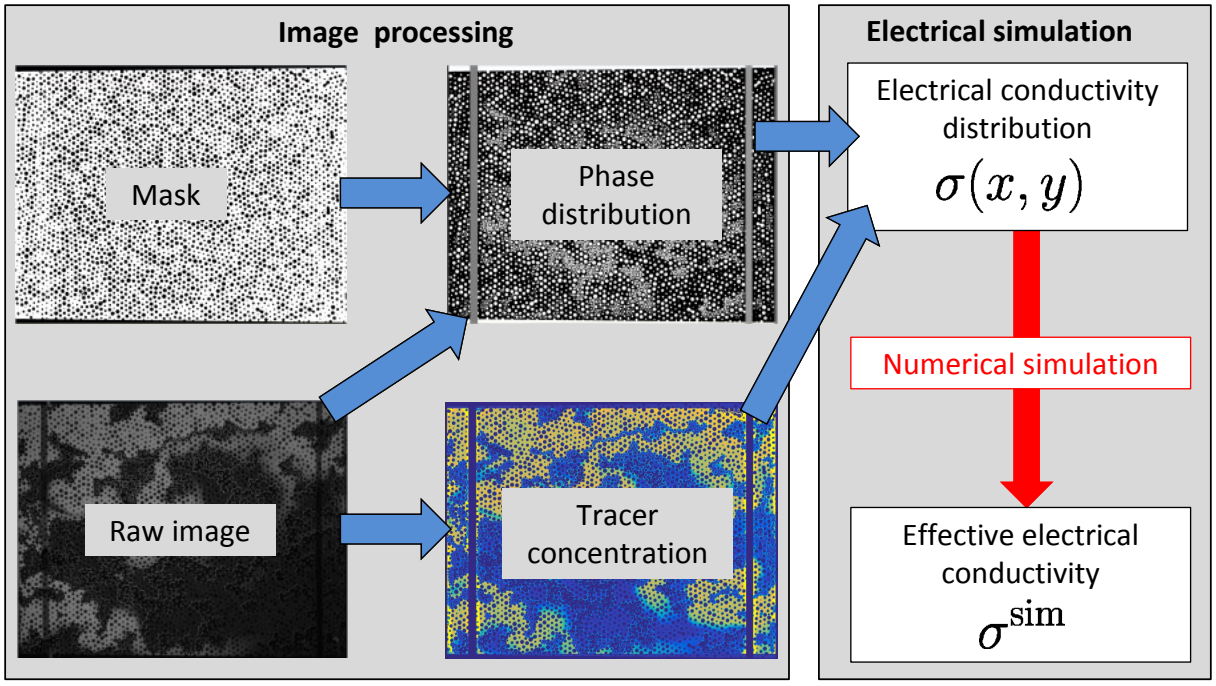

Figure 3: Schematic representation of the processing of the light-corrected images and the corresponding numerical simulation.

3.2 Petrophysical characterization

Many petrophysical relationships have been proposed to relate electrical conductivity to porosity, water saturation, and electrolyte concentration (e.g., Glover, 2015). The experiments described in section 2.3 provided various data sets of measured electrical conductivities σ^{meas} for different water saturations S_{w} at three different saline tracer conductivities σ_{w}. Figures 4a and b show σ^{meas} for different σ_{w} under saturated and partially saturated conditions, respectively.

Among the existing petrophysical relationships, let us consider the model that is the most used in the ERT literature: the classical model that is obtained by combining the so-called Archie's first and second law Archie (1942). It is applicable when the mineral surface conductivity can be neglected (i.e., typically for materials with low specific surface area such as sands or sandstones):

$$\sigma = \frac{S_{\text{w}}^n}{F}\sigma_{\text{w}}, \tag{1}$$

where σ and σ_{w} are the electrical conductivities (S m^{-1}) of the porous medium and pore-water, respectively, S_{w} is the water saturation (-), F is the electrical formation factor (-), and n is the saturation exponent (-). The electrical formation factor is related to porosity by a power law: $F = \phi^{-m}$ where m is the so-called cementation exponent. The parameters m and n depend on the pore-space and water phase geometry, respectively (e.g., Friedman, 2005). The petrophysical parameters obtained by optimization, using the Simplex algorithm (Caceci and Cacheris, 1984) and considering the entire dataset, are F = 1.85 and n = 4.

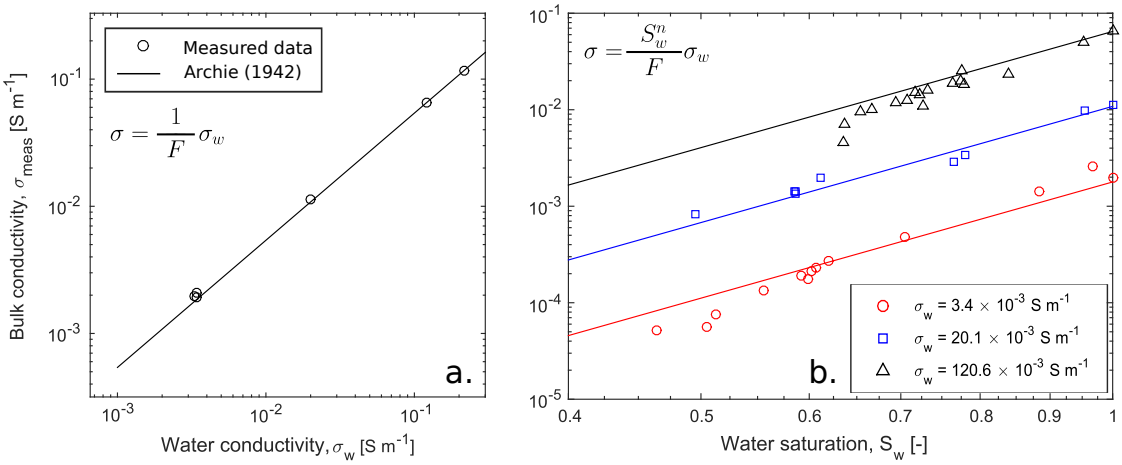

Figure 4: Bulk electrical conductivity as a function of (a) water conductivity in saturated conditions and (b) water saturation for different pore-water electrical conductivities. The dots (circles, squares, and triangles) correspond to the measurements (for different solutions) and the plain lines corresponds to the model of Archie (1942). The best fit to the entire data set was achieved with F = 1.85 and n = 4 in Eq. 1.

Equation (1) relating σ and σ_{w} allows us to reproduce very well the experimental data in saturated conditions (Fig. 4a), but the data fit is not as good for partially-saturated conditions (Fig. 4b). One likely reason for this is that the sample size is too small to produce a representative elementary volume for the experiments with the lowest water saturations.

Eq. (1) is based on the assumption that the pore water salinity is homogeneously distributed in the wetting phase. In the literature, ERT monitoring results of saline tracer tests are often interpreted by reformulating Eq. 1 and assuming that the water saturation is known. This results in an ERT-inferred electrical conductivity of the solute at the resolution scale:

$$\sigma_{\text{w}}^{\text{app}} = \frac{F}{S_{\text{w}}^n}\sigma^{\text{meas}}. \tag{2}$$

This apparent solute electrical conductivity can then be used to estimate an average solute concentration in the considered volume. For a spatially-constant F, S_w and n, $\sigma_\mathrm{w}^\mathrm{app}$ is theoretically limited by the Wiener bounds (Wiener, 1912), sometimes called Voigt and Reuss bounds.

The Wiener bounds are the arithmetic, $\bar{\sigma}_\mathrm{w}^\mathrm{a}$, and harmonic, $\bar{\sigma}_\mathrm{w}^\mathrm{h}$, means of the electrical conductivities σ_i constituting the wetting phase:

$$\bar{\sigma}_\mathrm{w}^\mathrm{a} = \frac{1}{N}\sum_{i=1}^{N}\sigma_\mathrm{w}^i, \tag{3}$$

$$\bar{\sigma}_\mathrm{w}^\mathrm{h} = \frac{N}{\sum_{i=1}^{N}\frac{1}{\sigma_\mathrm{w}^i}}, \tag{4}$$

where i denotes a single pixel belonging to the wetting phase and N is the total number of pixels identified as the wetting phase. The arithmetic and harmonic means are equivalent to the global conductivity of an electrical circuit where conductances would be placed either in parallel or in series, respectively. The Wiener bounds theory predicts that:

$$\bar{\sigma}_\mathrm{w}^\mathrm{a} \geq \sigma_\mathrm{w}^\mathrm{app} \geq \bar{\sigma}_\mathrm{w}^\mathrm{h}. \tag{5}$$

4 Results

This section describes and analyzes the data obtained from the laboratory tracer experiments (section 2) after data-processing following the workflow depicted in section 3.1. We first present the results from the tracer test in saturated conditions and then those obtained under partially-saturated conditions.

4.1 Tracer test under saturated conditions

Figure 5a shows the evolution of the measured bulk electrical conductivity during the tracer test performed in the water-saturated flow cell; $t = 0$ s corresponds to the beginning of the tracer injection in the cell. Figures 5b to e are snapshot images of the normalized tracer concentration at $t = 4000$ s, 6000 s, 8000 s, and 12000 s, respectively.

As expected, the measured bulk electrical conductivity increases as the tracer invades the medium. This increase is relatively smooth as a consequence of the tracer being transported according to an advection-diffusion process in a medium that is homogeneous at the Darcy scale. The tracer front is not perfectly straight nor transverse to the mean flow direction, due to some transverse heterogeneity in the conditions of tracer injection at the inlet of the medium, and possibly to a slight transverse permeability gradient in the medium. But no solute fingers are visible at scales smaller than a third of the flow cell width, and when the most advanced solute finger reaches the medium outlet, the most retarded region of the front has already reached half of the medium's length. Note that the rate of increase in the bulk electrical conductivity accelerates between $t = 4000$ and 8000 s (Fig. 5a), which corresponds to the time interval over which increasing tracer concentration is in contact with both potential electrodes (P1 and P2). The rate of increase decreases after $t = 8000$ s when a continuous strip of highly concentrated tracer joins the two electrodes. This enables electrical current to flow through the cell with a lesser resistance.

After post-processing the images and solving the electrical problem at each time step (see section 3.1), it is possible to compare the measured bulk conductivity (i.e., flow cell scale, or macroscopic scale) to the simulated ones. Figure 6a shows that the simulated conductivity (σ^sim) is in relatively good agreement with the data (σ^meas) measured at the cell scale (root mean square error: $RMSE$ = 0.0021 S m^{-1}).

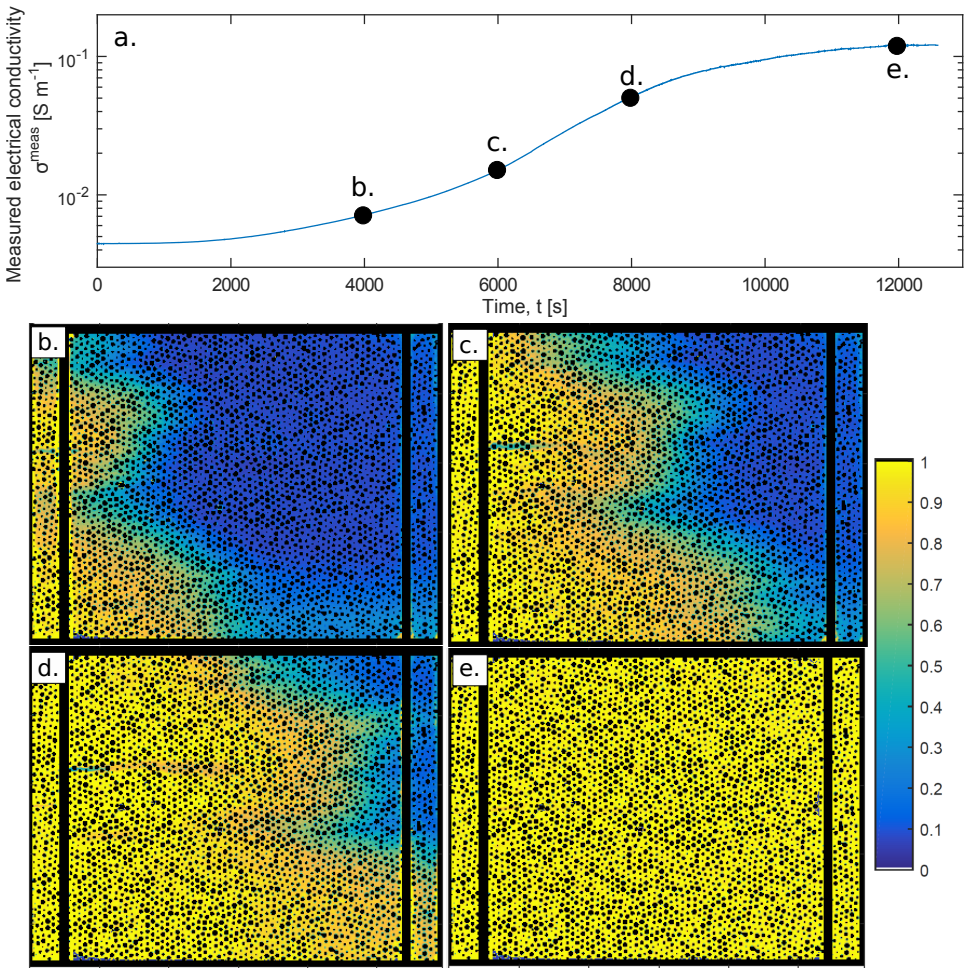

Figure 5: (a) Measured effective bulk electrical conductivity as a function of the time since the initiation of a tracer test in saturated conditions and corresponding images of the normalized tracer concentration in the flow cell at (b) $t = 4000$ s, (c) $t = 6000$ s, (d) $t = 8000$ s, and (b) $t = 12000$ s. The grains, the top and bottom boundaries, and the four electrodes appear as either black lines or circles on the image.

Figure 6b shows the evolution of the apparent electrical conductivity of the wetting phase $\sigma_{\mathrm{w}}^{\mathrm{app}}$ at the macroscopic scale (i.e., the scale of the flow cell) using Eq. 2. This value is compared to the arithmetic mean ("conductance in parallel" model) $\bar{\sigma}_{\mathrm{w}}^{\mathrm{a}}$ and to the harmonic mean ("conductance in series" model) $\bar{\sigma}_{\mathrm{w}}^{\mathrm{h}}$, showing that Eq. 5 is respected. Initially, $\sigma_{\mathrm{w}}^{\mathrm{app}}$ tends to follow the conductance in series model ($\bar{\sigma}_{\mathrm{w}}^{\mathrm{h}}$) until fluid carrying a significant concentration of the tracer reaches the second potential electrode P2 (between $t = 3000$ s and $t = 9000$ s). Then, $\sigma_{\mathrm{w}}^{\mathrm{app}}$ starts to follow the conductance in parallel model ($\bar{\sigma}_{\mathrm{w}}^{\mathrm{a}}$) as the tracer tends to be distributed more homogeneously in the pore space. Note that at the end of the tracer test, the pore space is not filled homogeneously by the tracer ($\bar{\sigma}_{\mathrm{w}}^{\mathrm{a}} \neq \bar{\sigma}_{\mathrm{w}}^{\mathrm{h}}$). Even with this homogeneous grain distribution, some parts of the medium are left with comparatively low tracer concentrations (Fig. 5e).

4.2 Tracer test under partially-saturated conditions

The same procedure was applied to the data obtained from the two-phase flow tracer test. Figure 7a shows the evolution of the measured electrical conductivity during the tracer test, while Figs. 7b, c, and d are snapshot images of the normalized tracer concentration at times $t = 2000$ s, 4000 s, 8000 s, and 14000 s after the beginning of the tracer injection in the cell, respectively. The non-wetting phase (air) appears in white, while the grains, boundaries, and electrodes appear in black. The air

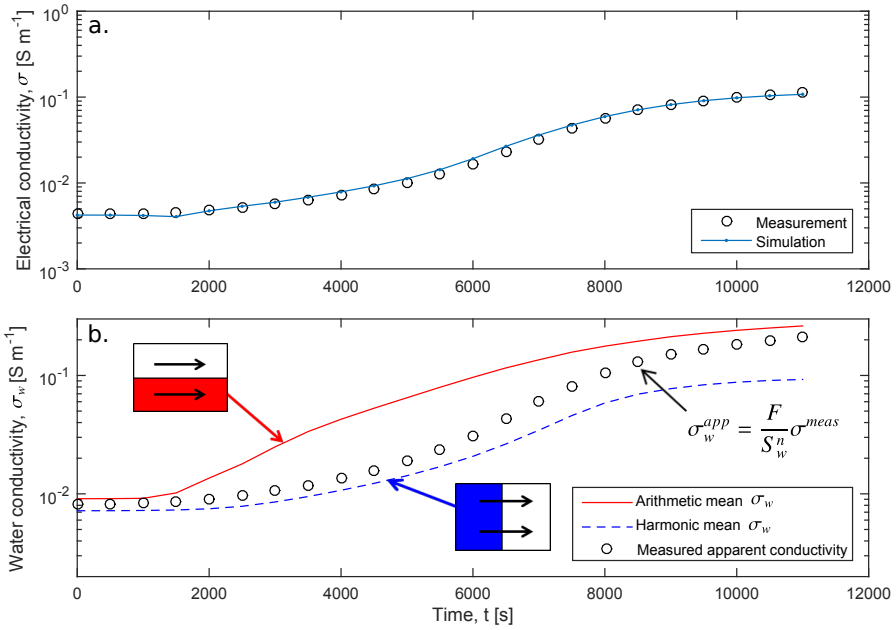

Figure 6: (a) Comparison between measured and simulated electrical conductivities at the scale of the flow cell under saturated conditions ($RMSE$ = 0.0021 S m^{-1}). (b) Apparent water electrical conductivity from Eq. 2 (with $F = 1.85$) and Wiener bound values of the wetting phase at the flow cell scale.

phase is arranged in clusters with a geometry that changed during the course of the experiment (i.e., a saturation increase from S_w= 0.69 to 0.87). Note that the strategy described in Section 3.1 allows us to account for these saturation changes in the simulations.

As for the saturated case, Figure 7a shows a strong increase in the bulk electrical conductivity as the tracer invades the medium. However, this increase is sharper and it appears earlier than for the saturated case. In partially saturated conditions, the tracer has a much reduced freedom to choose its pathway through the medium as not only grains act as obstacles to flow (as in the saturated case), but also large air clusters (e.g., Jiménez-Martínez et al., 2015). The path for the tracer includes more obstacles (grains + air clusters), having a higher mean interstitial velocity. This results in a larger heterogeneity of the tracer concentration in the flow cell.

In agreement with the experiment under saturated conditions (see Section 4.1), a sharp increase in the effective bulk electrical conductivity occurs when the tracer connects the P1 and P2 electrodes, creating a preferential pathway of least resistance for the electrical current (around $t = 4000$ s). One can also identify a second smaller increase around $t = 9000$ s when other fingers of tracer reach the P2 electrodes, thereby, creating new preferential pathways for the electrical current. The initial small fingering feature occurring at the top of the cell (Fig. 7c) generates a larger relative increase in σ^{meas} (from 10^{-3} to 10^{-2} S m^{-1} between $t = 2000$ s and $t = 6000$ s) than the larger fingers of tracer that can be seen in Fig. 7d (from 10^{-2} to 2×10^{-2} S m^{-1}). Fingering thus leads to strong increases in the electrical conductivity.

Figure 8a shows the comparison between the measured and the simulated electrical conductivities at the scale of the flow cell. The match between the simulation and the measurements, obtained with the same calibration curve as for the saturated experiment, is relatively good except at the beginning ($RMSE = 0.0017$ S m^{-1}). The small discrepancy could be explained by the fact that the optical contrast between the background solution and the air is somewhat too low in comparison to the in-

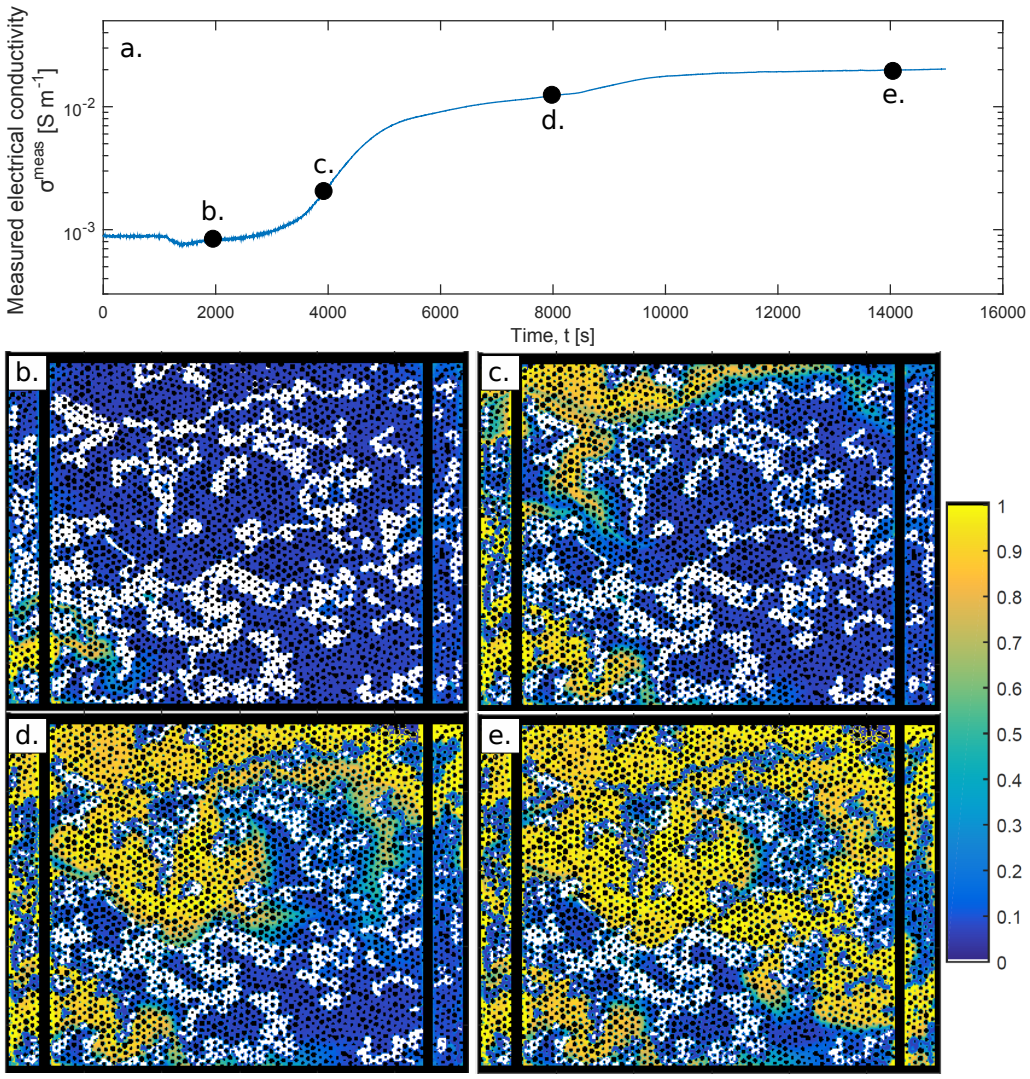

Figure 7: (a) Measured effective bulk electrical conductivity as a function of the time during a tracer test in partially saturated conditions and corresponding images of the normalized tracer concentration in the test cell at (b) $t = 2000$ s, (c) $t = 4000$ s, (d) $t = 8000$ s, and (e) $t = 14000$ s. The grains, the top and bottom boundaries, and the four electrodes appear as either black lines or circles on the image. The air appears in white clusters since there is no fluorescein in this phase. During the course of the experiment, the water saturation increased from $S_w = 0.69$ to 0.87.

tensity range corresponding to the heterogeneity of the lighting setup, so that even after correcting the images for lightning heterogeneity a small number of the air clusters are not detected as such, but are attributed to the background solution. The apparent electrical conductivity of the wetting phase at the macroscopic scale (i.e., the medium's scale or flow cell scale), σ_w^{app}, was calculated using Eq. 2 and considering the water saturation obtained from the image processing (Fig. 8a) and the best fit parameters from the petrophysical characterization ($F = 1.85$ and $n = 4$, see Fig. 4). Note that the data respect Eq. 5 during most of the tracer test duration, except at for some points at the beginning of the test. $\sigma_w^{app} > \bar{\sigma}_w^{a}$ (before t = 1500 s) and $\sigma_w^{app} < \bar{\sigma}_w^{h}$ (for t = 2500 and 3000 s) can be explained by the poor fit between the measured and simulated electrical conductivities at the corresponding times. Similarly to the saturated case, σ_w^{app} first tends to follow the "conductance in series" model before the first tracer finger connects P1 and P2 (Fig. 7c). Then, σ_w^{app} tends towards the "conductance in parallel" model but never reaches its values. Indeed, throughout the tracer test, the medium never reaches a homogenized distribution of tracer concentration over the time of the experiment. Figure 7e clearly shows the very heterogeneous nature of the tracer distribution after $t = 14000$ s, which explains why

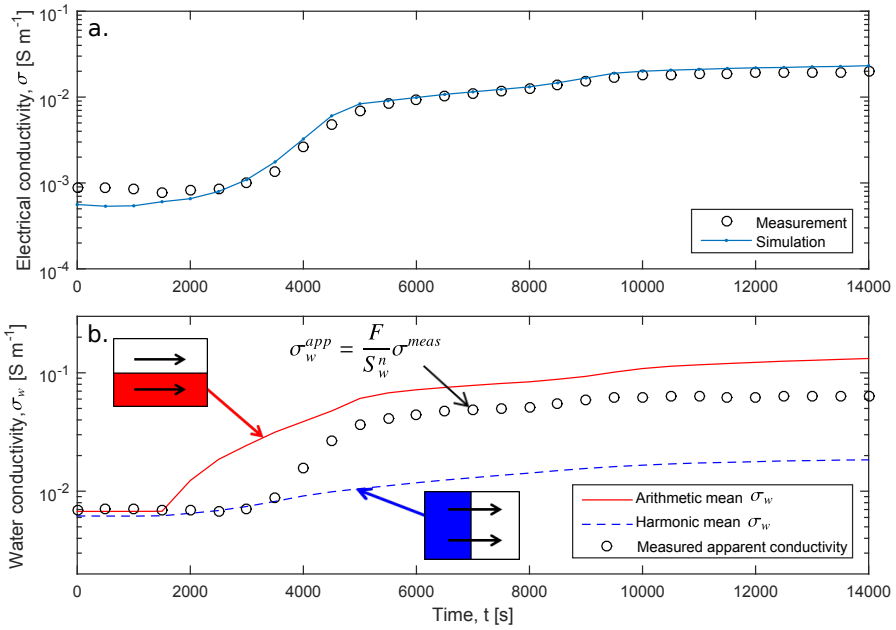

Figure 8: (a) Comparison between measured and simulated electrical conductivities at the scale of the flow cell under partially saturated conditions ($RMSE$ = 0.0017 S m^{-1}). (b) Apparent water electrical conductivity from Eq. 2 (with $F = 1.85$ and $n = 4$) and Wiener bound values of the wetting phase at the flow cell's scale. Note that the water saturation increased from $S_{\mathrm{w}} = 0.69$ to 0.87 during the test.

$\bar{\sigma}^{\mathrm{h}}_{\mathrm{w}}$ does not converge to $\bar{\sigma}^{\mathrm{a}}_{\mathrm{w}}$. The homogeneization might occur after a much longer time through diffusion processes along the concentration gradients. Ionic diffusion processes have very slow kinetics (of order $D = 10^{-10}$ m^2 s^{-1}) compared to the advection processes studied here: taking the linear size of the largest air clusters, $l_{\mathrm{air}} \simeq L/4 = 40$ mm as a typical length scale, the time necessary for the concentration to fully homogenize by ionic diffusion would be $l^2_{\mathrm{air}}/D = 1.6 \times 10^7$ s $= 185$ days.

5 Discussion

5.1 Petrophysical characterization of the 2D medium

The petrophysical characterization of the analogous 2D porous medium is an important step for the interpretation of the present experiments. F = 1.85 and n = 4 can seem surprising for petrophysicists used to natural rocks. The low value of the formation factor is a consequence of the large porosity, and the high value of the exponent n is the consequence of the 2D nature of the media under investigation (see the 2D pore network study of Maineult et al., 2018). Based on Archie (1942), the electrical tortuosity of the wetting phase, α_{w}, can be defined as (Revil and Jougnot, 2008):

$$\alpha_{\mathrm{w}} = \phi F S_{\mathrm{w}}^{(1-n)}, \tag{6}$$

which yields α_{w} = 1.35 and α_{w} = 4.04 at the beginning of the saturated and partially saturated tracer tests, respectively. These small tortuosities can be visualized by considering the phase distributions (e.g., only 2D obstacles, long continuous path of wetting phase, see Figs. 5 and 7). Note that the electrical tortuosity of the water phase determined by electrical conductivity measurements can be used to predict different transport properties of interest in hydrology, such as the ionic and gas diffusion

coefficients (e.g., Revil and Jougnot, 2008; Jougnot et al., 2009; Hamamoto et al., 2010) or thermal conductivity (e.g., Revil, 2000; Jougnot et al., 2010b).

Figure 4 shows that the fit of Archie's model for data obtained at full saturation is better than the fit obtained under partially saturated conditions. This can be explained by considering the concept of Representative Elementary Volume (REV): the smallest volume over which a measurement can be made to obtain a value representative of the whole (Hill, 1963). For saturated conditions with a homogeneous solution concentration (Fig. 4a), we conducted numerical tests by calculating the bulk conductivity σ^{calc} of only parts of the cell (not shown here). These tests showed that the difference between the bulk electrical conductivity calculated over a quarter of the cell and over the entire domain was smaller than 1.26 $\%$. Thus demonstrating that the REV of the saturated medium REV^{sat} is smaller than the flow cell. However, substantial differences between sub-domains occurred when we conducted a similar numerical study on the partially saturated medium. Therefore, the size of REV for the partially saturated medium, REV^{unsat} is likely larger than the size of the cell itself. This is expected as the linear size of the largest air clusters in the medium is of about half of the medium size. Consequently, we illustrate here the following inequality:

$$REV^{\text{sat}} \ll REV^{\text{unsat}}. \tag{7}$$

This is well-known in the literature (e.g., Joekar-Niasar and Hassanizadeh, 2011), but it is not always accounted for in hydrogeophysical studies. The limitations of Archie's law in the presence of percolation phenomena are discussed, for instance, by Kozlov et al. (2012).

5.2 Relationship between the concentration field and the measured conductivity

As shown in section 4, the heterogeneity of the tracer concentration field strongly depends on the saturation of the medium. Indeed, the concentration field is much more heterogeneous under partially saturated conditions than in the saturated case. As seen in Fig. 7d, at the end of the experiment ($t =$ 14000 s), large parts of the cell are still at the background solution concentration and the tracer is far from being homogeneously distributed. Note that molecular/ionic diffusion effects will eventually homogenize the tracer concentration but with very slow kinetics (see discussion in Jiménez-Martínez et al., 2015)).

Figure 9 compares the normalized tracer concentration distribution at a late stage of saturated and partially-saturated tracer tests and the corresponding simulated electrical current densities. The impact of the saturation distribution has a strong effect on the tracer distribution (Figs. 9a and b) that clearly manifest itself in simulated electrical current densities in saturated (Fig. 9c) and partially-saturated (Fig. 9d) conditions. In the fully saturated media, we find a current density that is homogeneously-distributed in the pore space, while in the partially-saturated case it is highly channelized. We find that the current paths are straighter and less tortuous than the saline tracer distribution (Figs. 9c and d). As expected, while the saturated porous media shows a homogeneous distribution of current densities, the unsaturated porous media is characterized by a highly channelized current density field.

In our experimental results, we show that the effective bulk electrical conductivity at the scale of the flow cell carries information about transport processes occurring at smaller scales. Electrical conductivity is sensitive to the saline tracer distribution in the medium. Indeed, for both saturated and partially-saturated conditions, a very strong increase of the effective bulk electrical conductivity can be seen when the saline tracer connects electrodes P1 and P2 (Figs. 5 and 7). The connectivity of the tracer in the medium is illustrated by the Wiener bounds; the apparent water conductivity is initially analogous to a model of conductance in series before it starts to follow a model of conductances in parallel. This analysis is even more instructive in partially saturated conditions as the breakthrough of only one solute finger through the medium acts as a preferential path for the electrical current, yielding a very strong change in bulk electrical conductivity.

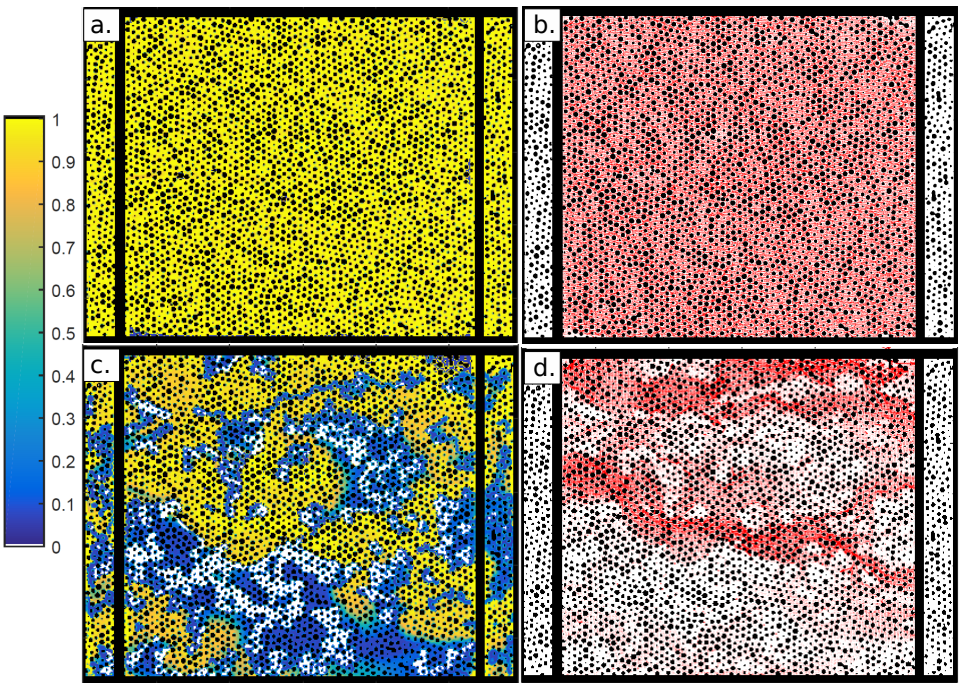

Figure 9: (a and c) Normalized tracer concentration and (b and d) current density spatial distribution at a late stage of the tracer test experiments under saturated (a and b correspond to $t = 12000$ s) and partially saturated (c and d correspond to $t = 14000$ s) conditions. Note that we only display the current density as red streamline density between P1 and P2, masking the effect of the high conductivity of the copper electrode to improve the readability of Figs. 9b and d.

Tracer fingers in the unsaturated case act as preferential paths for the electrical current (Fig. 9d) in comparison to the more homogeneous case in saturated conditions (Fig. 9b). One can identify “bottlenecks" as the places where the flow lines are focused between air clusters or grains (e.g., Jiménez-Martínez et al., 2015). This effect on the tracer transport affect the distribution of the electrical current flow (Fig. 9d). This channeling of the electrical current density is not only controlled by the tracer concentration alone, but also by how a region containing high tracer concentrations connects the different electrodes of the measurement setup. For example, the large tracer concentration area in the middle of Fig. 9d does not contribute significantly to the electrical flow.

The dynamics and evolution of the effective tracer percolation through the medium are also well captured by the bulk electrical conductivity. In saturated conditions, the smooth increase of σ during the entire tracer test corresponds to the progressive invasion of the flow cell by the saline tracer (Fig. 5). On the contrary, the more abrupt increase of σ around $t = 4000\ s$ and the smaller one around $t = 9000\ s$ (Fig. 7) denote the percolation of the first and second fingers of tracer through the porous medium. This clear link between tracer percolation and bulk electrical conductivity should be studied in more details to couple transport models at the pore-scale and hydrogeophysical measurements, for example following the idea proposed by Kemna et al. (2002) at the field-scale.

5.3 Electrical conductivity anisotropy

From the previous subsection, it appears that the bulk electrical conductivity is strongly related to the liquid phase connectivity and to the spatial distribution of the tracer concentration. It is therefore highly sensitive to the orientation of the electrical conductivity measurement setup with respect to the tracer transport. In order to study this effect, numerical tests have been performed: for each time step, the simulated bulk electrical conductivity presented in sections 4.1 and 4.2 (the longitudinal bulk electrical conductivity) has been compared to the value obtained from a numerical simulation where

the current flows in the medium from top to bottom, so that we compute the transverse bulk electrical conductivity. That is, we extracted the section of the images between electrode P1 and P2 (i.e., the investigation zone) and solved the electrical problem after imposing a 90° rotation to the porous medium around its center, without modifying the position of the electrodes. Figures 10a and b illustrate the simulation set-up of this anisotropy study, while Fig. 10c and d show the anisotropy factor λ of the electrical conductivity during the saturated and the partially saturated tracer tests, respectively. The dimensionless anisotropy factor, λ, is calculated as follows (e.g., Linde and Pedersen, 2004):

$$\lambda = \sqrt{\frac{\sigma^{\text{sim}}}{\sigma_{90}^{\text{sim}}}}, \tag{8}$$

where σ^{sim} and σ_{90}^{sim} are the longitudinal and the transverse electrical conductivities with respect to the fluid flow direction, respectively. Finally, Figures 10e and f are conceptual illustrations of ERT measurements for a lateral or vertical tracer test in the near surface, respectively.

The behaviour of the electrical anisotropy factor is completely different under saturated and partially saturated conditions (Fig. 10). Under saturated conditions (Fig. 10b), the bulk electrical conductivity of the medium is isotropic (i.e., $\lambda \simeq 1$) at the beginning and at the end of the tracer test. During the tracer test, the transverse electrical conductivity is higher than the longitudinal one as the zone that is invaded by the tracer create a high conductivity path for the electrical current from top to bottom (Fig. 5). On the contrary, under partially saturated, the medium is already anisotropic due to the presence of air clusters, the largest of which have a linear size close to half the medium size. Given the flow direction in the cell, air clusters tend to be more elongated in the longitudinal direction (Fig. 7), which yield $\sigma^{\text{sim}} > \sigma_{90}^{\text{sim}}$ ($\lambda = 1.15$ for $t = 0$ s). Then, as the tracer propagates in the pore space, the complex patterns of tracer fingering tend to increase the anisotropy factor (up to $\lambda = 2.41$). Note that, at the end of the tracer test, the anisotropy factor diminishes but does not return to its initial value (e.g., $\lambda = 1.59$ at $t = 14000$ s). This is caused by the remaining strong heterogeneity in the tracer concentration distribution (Fig. 9).

5.4 Impact on ERT interpretations

This study presents a new geoelectrical milli-fluidic setup that helps understanding better the link between state variables of hydrogeological interest (water saturation, flow velocity field, ionic concentration field, solute concentration field) and measurable upscaled geophysical properties under dynamic conditions. Considering that the scale of the flow cell in our experiment could be seen as an analogue to the resolution scale in a field ERT experiment, the present work has clearly shown that the apparent water electrical conductivity at the resolution scale is largely determined by the heterogeneity of ionic concentrations below this resolution scale, especially under partially saturated conditions (see Figs. 5 to 9).

Electrical conductivities resulting from ERT inversion are subjected to two kinds of processes masking the medium heterogeneity: (1) a smoothing above the cell size used to discretize the subsurface that is due to the inversion regularization imposed to make the inverse problem unique and (2) the conductivity homogenization at the REV (or discretized cell size) scale that we study herein. The inversion smoothing is the most scrutinized one as it is due to a regularization process needed to perform the inversion (e.g., Constable et al., 1987). Various works have described and studied the impact of model regularization, showing that information about sharp contrasts between model cells is lost (see, among other works: Day-Lewis et al., 2005; Singha and Gorelick, 2006). This phenomenon induces an apparent tracer loss when conducting in situ ERT monitoring of tracer tests. The second process masking the heterogeneity of the processes at play is a consequence of unaccounted saline tracer heterogeneity below the cell size used in the inversion. This cell size is often implicitly assumed to correspond to the REV scale and petrophysical models are used (see Eq. 1) that assumes that saline tracer heterogeneity is constant. Only a few works have considered tracer heterogeneity at

the REV scale (e.g., Singha et al., 2007; Day-Lewis et al., 2017)), but only for two classes of porosities. Future work is needed to ensure proper upscaling to the cell size used in geophysical inversion and forward modeling. This work has clearly demonstrated that such effects can be very strong. In practice, we suggest that both of these effects are interconnected and we refer to them collectively as sub-resolution effects.

In our experiments we find that the heterogeneous fluid phase distributions and ionic concentration field in the aqueous phase at the sub-resolution scale have shown a strong impact on the effective bulk electrical conductivity. When conducting ERT monitoring, researchers often try to retrieve the ionic concentration at the resolution scale from the bulk electrical conductivity using a petrophysical relationship (often Archie, 1942, Eqs. 1 and 2) which assume a homogeneous distribution of σ_{w} below the resolution scale. Thus, they ignore the two effects described above (regularization and homogenization). However, in section 4, we have shown that the bulk electrical conductivity measured at the scale of our porous medium depends strongly on the connectivity of the tracer between the two potential electrodes at the pore-scale. Figures 6b and 8b show that as long as the medium is not homogeneous, the apparent water conductivity can be much smaller than the arithmetic mean of its constituents: $\sigma_{\mathrm{w}}^{\mathrm{app}} \ll \bar{\sigma}_{\mathrm{w}}^{\mathrm{a}}$. Indeed, the electrical current is only sensitive to a fraction of the tracer in the medium, the part connecting both sides of the voxel in the direction of the electrical current, as shown by Fig. 9. And, as discussed previously, the time of homogeneization can be much longer than the duration of an experiment (be it a lab or a field experiment). This inequality between effective bulk conductivity and arithmetic average conductivity results in an apparent mass loss when inferring solute concentrations from ERT inversion results using Eq. (2). Indeed, in our medium, the arithmetic mean of the local conductivities (the upper Wiener bound), $\bar{\sigma}_{\mathrm{w}}^{\mathrm{a}}$, is proportional to the arithmetic mean of local concentrations, which is the solute concentration defined at the medium scale. If one considers that our medium scale represents the resolution scale of an ERT field experiment (Figs. 10e and f), the solute concentration measured by ERT would be inferred from an apparent water conductivity measured at that scale, and hence its ratio to the true solute concentration would equal the ratio $\sigma_{\mathrm{w}}^{\mathrm{app}}/\bar{\sigma}_{\mathrm{w}}^{\mathrm{a}}$. In other words the apparent mass loss is a necessary consequence of the upper Wiener bound at sub-resolution scale and is to be expected as soon as the solute is not well-mixed in the pore space and at the ERT resolution scale (i.e., always). This mechanism could account for an important proportion of the very important mass loss in ERT studies (e.g., 75 $\%$ of apparent mass loss in Singha and Gorelick (2005)). Furthermore, these results indicate that monitoring an horizontal tracer flow (Fig. 10e) or a vertical one (Fig. 10f) from the surface could result in very different apparent mass losses, depending also on the type of ERT measurements performed (surface measurements or borehole measurements). The use of electrode arrays at both the surface and in boreholes (e.g., Looms et al., 2008), when available, could help better constraining the tracer flow direction by taking advantage of this anisotropy.

Finally, to the best of our knowledge, the electrical conductivity has never been considered a tensor in time-lapse ERT inversions (see LaBrecque and Casale, 2002; Pain et al., 2003, for static inversion). Therefore, the effect of tracer percolation on the electrical conductivity anisotropy factor is largely ignored and will inevitably produce artifacts. Given the large value obtained in the anisotropy test (up to $\lambda = 2.76$ in Fig. 10d), it seems that describing electrical conductivity as a tensorial property during tracer tests should be investigated in more details.

5.5 Technical improvements for further experiments

We have developed a geoelectrical milli-fluidic setup to study sub-resolution effects associated with electrical conductivity monitoring of tracer tests. Even if this initial study is already rich in results, significant improvements could be made to the experimental setup and measurement protocol.

The opacity of the currently used electrodes has the disadvantage of degrading the information available about what is happening above them (Figs. 5, 7, and 9), making for example the determination of air cluster boundaries above an electrode difficult. Different possibilities can be explored to

solve this issue, among which the use of transparent electrodes, or locating the electrodes outside of the porous medium.

An appropriate choice of fluorescein concentration in the injected solutions is crucial to obtain high-quality images with a suitable optical contrast. For future works, we recommend that the background solution should be more concentrated in fluorescein, in order to improve the contrast between the liquid phase at low fluorescein concentration and the air phase. Furthermore, the mass concentration ratio between fluorescein and NaCl salt should be revisited to take advantage of the largest range of light intensity possible. We anticipate that performing the calibration of the transfer function between light intensity and local conductivity in the same flow cell as that used for the tracer experiments will remove the need for an a posteriori correction of the calibration curve. Besides, the use of many more calibration points will help improving the reliability of that curve.

6 Conclusion

We propose a new geoelectrical milli-fluidic setup to study the impact of the pore-scale distribution of fluid phases and tracer concentrations on the effective bulk electrical conductivity. The setup is based on a two-dimensional porous medium consisting of a single layer of cylindrical grains positioned randomly between two parallel glass plates. The macroscopic scale in our laboratory study can be seen as an analogue to the resolution scale of ERT at the field-scale. After performing a petrophysical characterization of the porous medium, we monitored variations in the bulk electrical conductivity of the porous medium during saline tracer tests under full and partial saturation. We find that the air distribution and the resulting heterogeneity in solute concentrations lead to electrical current channeling with strong effects on effective bulk conductivities. This suggests a strong impact of pore-scale and sub-resolution effects on upscaled bulk electrical conductivity in terms of magnitude and anisotropy. Such effects are expected to systematically occur at the field-scale due to incomplete solute mixing below the resolution scale. We suggest that they could contribute significantly to an important inconsistency in conventional time-lapse ERT image processing, namely the apparent loss of tracer mass. In fact, the use of the upper Wiener bound of the effective bulk electrical conductivity implies that the inferred solute concentration at the ERT resolution scale will always be smaller than the true average solute concentration at that scale. The presented geoelectrical milli-fluidic setup (and variations thereof) opens up a range of opportunities to investigate the link between electrical signals and a variety of pore-scale processes, such as mixing, reactive transport, and biogeochemical reactions.

Acknowledgment

The authors gratefully acknowledge support from the EC2CO program of INSU/CNRS (project AO2014-906387). The experimental work was also supported by the Interreg project CLIMAWAT, EU-RDF INTERREG IVA France (Channel)-England program. The data used are available by contacting the corresponding author. The authors gratefully thank the editor, Kamini Singha, and an anonymous reviewer for their very constructive comments.

References

References

de Anna, P., Jimenez-Martinez, J., Tabuteau, H., Turuban, R., Le Borgne, T., Derrien, M., Méheust, Y.. Mixing and reaction kinetics in porous media: An experimental pore scale quantification. Environmental Science & Technology 2013;48(1):508–516.

Archie, G.. The electrical resistivity log as an aid in determining some reservoir characteristics. Transaction of the American Institute of Mining and Metallurgical Engineers 1942;146:54–61.

Binley, A., Cassiani, G., Middleton, R., Winship, P.. Vadose zone flow model parameterisation using cross-borehole radar and resistivity imaging. Journal of Hydrology 2002;267(3):147–159.

Binley, A., Cassiani, G., Revil, A., Titov, K., Vereecken, H.. Applied Hydrogeophysics. Springer, 2006.

Binley, A., Hubbard, S.S., Huisman, J.A., Revil, A., Robinson, D.A., Singha, K., Slater, L.D.. The emergence of hydrogeophysics for improved understanding of subsurface processes over multiple scales. Water Resources Research 2015;51(6):3837–3866.

Binley, A., Kemna, A.. Dc resistivity and induced polarization methods. In: Hydrogeophysics. Springer; 2005. p. 129–156.

Briggs, M.A., Day-Lewis, F.D., Ong, J.B., Curtis, G.P., Lane, J.W.. Simultaneous estimation of local-scale and flow path-scale dual-domain mass transfer parameters using geoelectrical monitoring. Water Resources Research 2013;49(9):5615–5630.

Briggs, M.A., Day-Lewis, F.D., Ong, J.B., Harvey, J.W., Lane, J.W.. Dual-domain mass-transfer parameters from electrical hysteresis: Theory and analytical approach applied to laboratory, synthetic streambed, and groundwater experiments. Water Resources Research 2014;50(10):8281–8299.

Caceci, M., Cacheris, W.. Simplex optimization algorithm. Byte 1984;5:340–351.

Constable, S.C., Parker, R.L., Constable, C.G.. Occam's inversion: A practical algorithm for generating smooth models from electromagnetic sounding data. Geophysics 1987;52(3):289–300.

Daily, W., Ramirez, A., LaBrecque, D., Nitao, J.. Electrical resistivity tomography of vadose water movement. Water Resources Research 1992;28(5):1429–1442.

Day-Lewis, F.D., Linde, N., Haggerty, R., Singha, K., Briggs, M.A.. Pore network modeling of the electrical signature of solute transport in dual-domain media. Geophysical Research Letters 2017;44(10):4908–4916. 2017GL073326.

Day-Lewis, F.D., Singha, K., Binley, A.M.. Applying petrophysical models to radar travel time and electrical resistivity tomograms: Resolution-dependent limitations. Journal of Geophysical Research: Solid Earth 2005;110(B8):B08206.

Dentz, M., Le Borgne, T., Englert, A., Bijeljic, B.. Mixing, spreading and reaction in heterogeneous media: A brief review. Journal of Contaminant Hydrology 2011;120:1–17.

Doetsch, J., Linde, N., Vogt, T., Binley, A., Green, A.G.. Imaging and quantifying salt-tracer transport in a riparian groundwater system by means of 3D ERT monitoring. Geophysics 2012;77(5):B207–B218.

Ferrari, A., Jimenez-Martinez, J., Borgne, T.L., Méheust, Y., Lunati, I.. Challenges in modeling unstable two-phase flow experiments in porous micromodels. Water Resources Research 2015;51(3):1381–1400.

Ferrari, A., Lunati, I.. Direct numerical simulations of interface dynamics to link capillary pressure and total surface energy. Advances in Water Resources 2013;57:19–31.

Friedel, S.. Resolution, stability and efficiency of resistivity tomography estimated from a generalized inverse approach. Geophysical Journal International 2003;153(2):305–316.

Friedman, S.P.. Soil properties influencing apparent electrical conductivity: a review. Computers and electronics in agriculture 2005;46(1):45–70.

Glass, R., Nicholl, M.. Physics of gravity fingering of immiscible fluids within porous media: An overview of current understanding and selected complicating factors. Geoderma 1996;70(2-4):133–163.

Glover, P.. Geophysical properties of the near surface earth: electrical properties. Treatise on Geophysics 2015;11:89–137.

Guérin, R.. Borehole and surface-based hydrogeophysics. Hydrogeology Journal 2005;13(1):251–254.

Haarder, E.B., Jensen, K.H., Binley, A., Nielsen, L., Uglebjerg, T., Looms, M.. Estimation of recharge from long-term monitoring of saline tracer transport using electrical resistivity tomography. Vadose Zone Journal 2015;14(7):1–13.

Hamamoto, S., Moldrup, P., Kawamoto, K., Komatsu, T.. Excluded-volume expansion of Archie's law for gas and solute diffusivities and electrical and thermal conductivities in variably saturated porous media. Water Resources Research 2010;46(6).

Hassanizadeh, S.M., Celia, M.A., Dahle, H.K.. Dynamic effect in the capillary pressure–saturation relationship and its impacts on unsaturated flow. Vadose Zone Jounal 2002;1(1):38–57.

Hill, R.. Elastic properties of reinforced solids: Some theoretical principles. Journal of the Mechanics and Physics of Solids 1963;11(5):357 – 372.

Hubbard, S., Linde, N.. Hydrogeophysics. In: Wilderer, P., editor. Treatise on Water Science. Oxford: Academic Press; volume 1; 2011. p. 401–434.

Hubbard, S.S., Rubin, Y.. Introduction to hydrogeophysics. In: Hydrogeophysics. Springer; 2005. p. 3–21.

Jiménez-Martínez, J., de Anna, P., Tabuteau, H., Turuban, R., Borgne, T.L., Méheust, Y.. Pore-scale mechanisms for the enhancement of mixing in unsaturated porous media and implications for chemical reactions. Geophysical Research Letters 2015;42(13):5316–5324.

Jiménez-Martínez, J., Le Borgne, T., Tabuteau, H., Méheust, Y.. Impact of saturation on dispersion and mixing in porous media: Photobleaching pulse injection experiments and shear-enhanced mixing model. Water Resources Research 2017;53:1457–1472.

Joekar-Niasar, V., Hassanizadeh, S.M.. Specific interfacial area: The missing state variable in two-phase flow equations? Water Resources Research 2011;47:W05513.

Jougnot, D., Ghorbani, A., Revil, A., Leroy, P., Cosenza, P.. Spectral induced polarization of partially saturated clay-rocks: A mechanistic approach. Geophysical Journal International 2010a;180(1):210–224.

Jougnot, D., Revil, A., Leroy, P.. Diffusion of ionic tracers in the callovo-oxfordian clay-rock using the donnan equilibrium model and the formation factor. Geochimica et Cosmochimica Acta 2009;73(10):2712–2726.

Jougnot, D., Revil, A., et al. Thermal conductivity of unsaturated clay-rocks. Hydrology and Earth System Sciences 2010b;14(1):91–98.

Kemna, A., Kulessa, B., Vereecken, H.. Imaging and characterisation of subsurface solute transport using electrical resistivity tomography (ERT) and equivalent transport models. Journal of Hydrology 2002;267(3):125–146.

Koestel, J., Larsbo, M.. Imaging and quantification of preferential solute transport in soil macropores. Water Resources Research 2014;50(5):4357–4378.

Kozlov, B., Schneider, M., Montaron, B., Lagues, M., Tabeling, P.. Archie's law in microsystems. Transport in Porous Media 2012;:1–20.

Künze, R., Lunati, I.. An adaptive multiscale method for density-driven instabilities. Journal of Computational Physics 2012;231(17):5557–5570.

LaBrecque, D.J., Casale, D.. Experience with anisotropic inversion for electrical resistivity tomography. In: 15th EEGS Symposium on the Application of Geophysics to Engineering and Environmental Problems. 2002. .

Le Borgne, T., Dentz, M., Davy, P., Bolster, D., Carrera, J., De Dreuzy, J.R., Bour, O.. Persistence of incomplete mixing: A key to anomalous transport. Physical Review E 2011;84(1):015301.

Linde, N., Pedersen, L.B.. Evidence of electrical anisotropy in limestone formations using the RMT technique. Geophysics 2004;69(4):909–916.

Looms, M.C., Jensen, K.H., Binley, A., Nielsen, L.. Monitoring unsaturated flow and transport using cross-borehole geophysical methods. Vadose Zone Journal 2008;7(1):227–237.

Løvoll, G., Jankov, M., Måløy, K.J., Toussaint, R., Schmittbuhl, J., Schäfer, G., Méheust, Y.. Influence of viscous fingering on dynamic saturation-pressure curves in porous media. Transport in Porous Media 2011;86:305–324.

Maineult, A., Jougnot, D., Revil, A.. Variations of petrophysical properties and spectral induced polarization in response to drainage and imbibition: a study on a correlated random tube network. Geophysical Journal International 2018;(ggx474).

Méheust, Y., Løvoll, G., Måløy, K.J., Schmittbuhl, J.. Interface scaling in a two-dimensional porous medium under combined viscous, gravity, and capillary effects. Physical Review E 2002;66(5):051603.

Menke, W.. Geophysical Data Analysis: Discrete Inverse Theory. International Geophysics Series, New York: Academic Press, 1989, Rev ed 1989;1.

Pain, C.C., Herwanger, J.V., Saunders, J.H., Worthington, M.H., de Oliveira, C.R.. Anisotropic resistivity inversion. Inverse Problems 2003;19(5):1081.

Pollock, D., Cirpka, O.A.. Fully coupled hydrogeophysical inversion of a laboratory salt tracer experiment monitored by electrical resistivity tomography. Water Resources Research 2012;48(1):W01505.

Revil, A.. Thermal conductivity of unconsolidated sediments with geophysical applications. Journal of Geophysical Research 2000;105(B7):16749–16.

Revil, A., Jougnot, D.. Diffusion of ions in unsaturated porous materials. Journal of Colloid and Interface Science 2008;319(1):226–235.

Revil, A., Karaoulis, M., Johnson, T., Kemna, A.. Review: Some low-frequency electrical methods for subsurface characterization and monitoring in hydrogeology. Hydrogeology Journal 2012;:1–42.

Rosas-Carbajal, M., Linde, N., Peacock, J., Zyserman, F., Kalscheuer, T., Thiel, S.. Probabilistic 3-d time-lapse inversion of magnetotelluric data: application to an enhanced geothermal system. Geophysical Journal International 2015;203(3):1946–1960.

Schlumberger, C.. Etude sur la prospection electrique du sous-sol [Study on underground electrical prospecting]. Gauthier-Villars, 1920.

Seyfried, M., Rao, P.. Solute transport in undisturbed columns of an aggregated tropical soil: Preferential flow effects. Soil Science Society of America Journal 1987;51(6):1434–1444.

Singha, K., Day-Lewis, F.D., Lane, J.. Geoelectrical evidence of bicontinuum transport in groundwater. Geophysical Research Letters 2007;34(12).

Singha, K., Gorelick, S.M.. Saline tracer visualized with three-dimensional electrical resistivity tomography: Field-scale spatial moment analysis. Water Resources Research 2005;41(5):W05023.

Singha, K., Gorelick, S.M.. Effects of spatially variable resolution on field-scale estimates of tracer concentration from electrical inversions using archieï¿½s law. Geophysics 2006;71(3):G83–G91.

Singha, K., Pidlisecky, A., Day-Lewis, F.D., Gooseff, M.N.. Electrical characterization of non-fickian transport in groundwater and hyporheic systems. Water Resources Research 2008;44(4):W00D07.

Sjöback, R., Nygren, J., Kubista, M.. Absorption and fluorescence properties of fluorescein. Spectrochimica Acta Part A: Molecular and Biomolecular Spectroscopy 1995;51(6):L7–L21.

Swanson, R.D., Binley, A., Keating, K., France, S., Osterman, G., Day-Lewis, F.D., Singha, K.. Anomalous solute transport in saturated porous media: Relating transport model parameters to electrical and nuclear magnetic resonance properties. Water Resources Research 2015;51(2):1264–1283.

Tallakstad, K.T., Knudsen, H.A., Ramstad, T., Løvoll, G., Måløy, K.J., Toussaint, R., Flekkøy, E.G.. Steady-State Two-Phase Flow in Porous Media: Statistics and Transport Properties. Physical Review Letters 2009;102:074502.

Toussaint, R., Må løy K., K.J., Méheust, Y., Løvoll, G., Jankov, M., Schäfer, G., Schmittbuhl, J.. Two-phase flow: structure, upscaling, and consequences for macroscopic transport properties. Vadose Zone Journal 2012;11(3).

Wiener, O.. Theory of composite bodies. Abh sächs Ges Wiss 1912;33:507–525.

Willingham, T.W., Werth, C.J., Valocchi, A.J.. Evaluation of the effects of porous media structure on mixing-controlled reactions using pore-scale modeling and micromodel experiments. Environmental science & technology 2008;42(9):3185–3193.

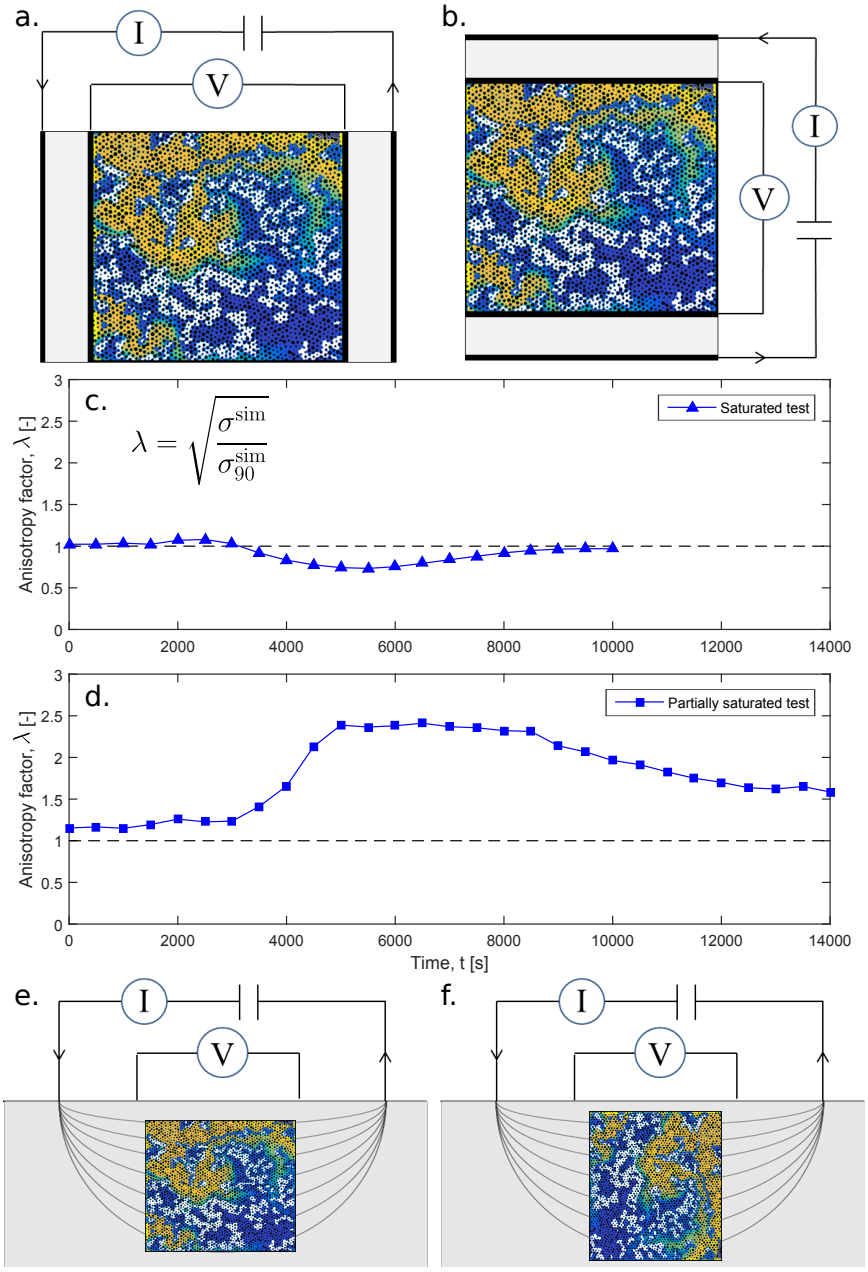

Figure 10: Numerical study of anisotropy in the effective bulk electrical conductivity during tracer experiments for (a) the experimental configuration with longitudinal electrical transport and (b) a rotation of the set of electrodes with respect to the medium by 90° (i.e., imposing transverse electrical transport with respect to the main flow direction). (c) The electrical anisotropy factor as a function of time during the saturated tracer test. (d) Same as (c) for partially saturated conditions. Note that the anistropy study is only conducted on the part of the cell between P1 and P2 (i.e., the investigation zone). The dashed line corresponds to the value λ =1. Conceptual view of surface-based ERT measurements for (e) lateral and (f) vertical tracer flow in the near surface.